Protein Structure and Folding:

Structure of a Conserved Golgi Complex-targeting Signal in Coronavirus Envelope Proteins

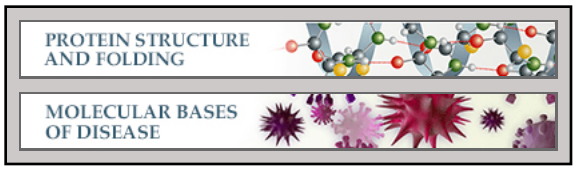

Yan Li, Wahyu Surya, Stephanie Claudine and Jaume Torres

J. Biol. Chem. 2014, 289:12535-12549.
doi: 10.1074/jbc.M114.560094 originally published online March 25, 2014

THE JOURNAL OF BIOLOGICAL CHEMISTRY VOL. 289, NO. 18, pp. 12535–12549, May 2, 2014

Structure of a Conserved Golgi Complex-targeting Signal in Coronavirus Envelope Proteins

Received for publication, February 24, 2014, and in revised form, March 13, 2014 Published, JBC Papers in Press, March 25, 2014, DOI 10.1074/jbc.M114.560094

Yan Li[1], **Wahyu Surya**[1], **Stephanie Claudine, and Jaume Torres**[2]

From the School of Biological Sciences, Nanyang Technological University, 60 Nanyang Drive, 637551 Singapore

Background: Coronavirus envelope (CoV E) proteins have a predicted β-coil-β motif reported to target the Golgi complex.
Results: This conserved domain forms β-structure on its own but is α-helical in the context of full-length SARS-CoV E protein.
Conclusion: This domain is potentially involved in large conformational transitions.
Significance: This is the first structural data of the extramembrane domain of any coronavirus E protein.

Coronavirus envelope (CoV E) proteins are ~100-residue polypeptides with at least one channel-forming α-helical transmembrane (TM) domain. The extramembrane C-terminal tail contains a completely conserved proline, at the center of a predicted β-coil-β motif. This hydrophobic motif has been reported to constitute a Golgi-targeting signal or a second TM domain. However, no structural data for this or other extramembrane domains in CoV E proteins is available. Herein, we show that the E protein in the severe acute respiratory syndrome virus has only one TM domain in micelles, whereas the predicted β-coil-β motif forms a short membrane-bound α-helix connected by a disordered loop to the TM domain. However, complementary results suggest that this motif is potentially poised for conformational change or in dynamic exchange with other conformations.

Coronaviruses (CoV[3]; order Nidovirales, family Coronaviridae, subfamily Coronavirinae) are enveloped viruses organized into three groups (1, 2)[4]: group 1 (α-coronaviruses), group 2 (β-coronaviruses) and group 3 (γ-coronaviruses). Coronaviruses have been known to cause common cold symptoms in humans and a variety of lethal diseases in birds and mammals (4). However, in 2003, the virus responsible for the severe acute respiratory syndrome (SARS-CoV) (5) produced a near pandemic with 8,273 cases and 775 deaths (6). In 2012, a novel β-coronavirus (HCoV-EMC) (7–9) was discovered that has already led to many fatalities (10–12).

The main coronavirus structural proteins are S (spike), E (envelope), M (membrane), and N (nucleocapsid), where S, E, and M are integral membrane proteins. E proteins are ~100-residue-long polypeptides that are minor components in virions but are abundantly expressed inside infected cells (13). They have a short hydrophilic N terminus, at least one predicted terminal transmembrane (TM) domain, and a less hydrophobic C-terminal tail.

Co-expression of E and M proteins is sufficient for formation and release of virus-like particles (14–19), and E proteins have been proposed to participate in inducing membrane curvature or in the scission of particles (20). Mutations at their C-terminal extramembrane domain impair viral assembly and maturation in the murine hepatitis virus (20). In the transmissible gastroenteritis virus, the absence of E protein resulted in a blockade of virus trafficking in the secretory pathway and prevention of virus maturation (21, 22). In the case of the severe acute respiratory syndrome coronavirus (SARS-CoV), viruses lacking the E gene showed attenuation and did not grow in the central nervous system (23, 24), whereas stress response genes were up-regulated and cell apoptosis increased (25). These results suggested a role of E protein in both tissue tropism and pathogenicity, where modulation of stress responses contributes to viral attenuation. In fact, SARS-CoV ΔE attenuated viruses constitute promising vaccine candidates (26–28). Thus, although E proteins are not absolutely essential for *in vitro* or *in vivo* coronavirus replication, their absence is clearly deleterious.

Immunofluorescence experiments have shown that SARS-CoV E has a cytoplasmically oriented C terminus and a lumenal N terminus (*i.e.* an $N_{exo}C_{cyto}$ orientation) (13), which is consistent with the presence of a single TM domain. SARS-CoV E protein and other CoV E proteins have channel activity in synthetic membranes (29–31). This channel activity is mediated by formation of pentameric oligomers (32–34) and is only very mildly selective for cations (35). The only available structural data for CoV E proteins, obtained using synthetic TM peptides, is derived from the channel-forming TM domain in SARS-CoV E (32, 34, 36). No structural data are available for the predicted N- or C-terminal extramembrane domains despite the latter being critical for viral assembly (37, 38), although some results have been obtained using shorter synthetic peptides encom-

[1] Both authors contributed equally to this work.
The atomic coordinates and structure factors (code 2MM4) have been deposited in the Protein Data Bank (http://wwpdb.org/).
Assigned chemical shifts have been deposited at the Biological Magnetic Resonance Bank (BMRB) with ID 19845.
[2] To whom correspondence should be addressed. Tel.: 65-6316-2857; Fax: 65-6791-3856; E-mail: jtorres@ntu.edu.sg.
[3] The abbreviations used are: CoV E, coronavirus envelope; SARS, severe acute respiratory syndrome; BisTris, 2-[bis(2-hydroxyethyl)amino]-2-(hydroxymethyl)propane-1,3-diol; PFO, perfluorooctanoic acid; H/D, hydrogen/deuterium; DMPC, 1,2-dimyristoyl-*sn*-glycero-3-phosphate; PRE, paramagnetic relaxation enhancement; MTSSL, (1-oxyl-2,2,5,5-tetramethyl-Δ^3-pyrroline-3-methyl) methanethiosulfonate; dMTSSL, (1-acetyl-2,2,5,5-tetramethyl-Δ^3-pyrroline-3-methyl) methanethiosulfonate; 5- and 16-DSA, 5- and 16-doxyl stearic acid, respectively; CSP, chemical shift perturbation; HMA, 5-(*N*,*N*-hexamethylene)amiloride; TM, transmembrane; FL, full-length.
[4] R. J. De Groot, J. Ziebuhr, L. L. Poon, P. C. Woo, P. Talbot, P. J. M. Rottier, K. V. Holmes, R. Baric, S. Perlman, L. Enjuanes, and A. E. Gorbalenya, Revision of the Family Coronaviridae. Taxonomic Proposal of the Coronavirus Study Group to the ICTV Executive Committee, unpublished data.

passing this domain (39). The C-terminal domain of E proteins contains a totally conserved proline residue, which in β- and γ-coronaviruses is at the center of a predicted β-coil-β motif (Fig. 1*A*), reminiscent of viral internal fusion peptides (40–42). In SARS-CoV E, this motif was found to be responsible for redirecting a plasma membrane protein to the Golgi region. Conversely, mutations designed to increase its α-helical propensity disrupted localization to membranes (43).

The C-terminal tail of E proteins is also important for its interaction with the C-terminal domain of M protein (18, 44, 45) at the cytoplasmic side of the endoplasmic reticulum-Golgi intermediate compartment, the budding compartment of the host cell. These interactions are the major drivers for envelope formation (46). The C-terminal tail of SARS-CoV E protein also interacts with the cellular protein PALS1 (47), which is thus depleted from the tight junctions in epithelial cells. Finally, SARS-CoV E interacts with the seven-domain (48) SARS nonstructural protein 3 (Nsp3) (49).

Thus, it is crucial to determine the structure of the C-terminal predicted extramembrane domain of E proteins, especially in the context of a large construct that includes the TM domain. Until now, these structural studies have been hampered by problems in expression, purification, and stabilization of E proteins. We report herein the first detailed structure of a truncated form of the SARS-CoV E monomer that includes both its TM domain and its predicted β-coil-β motif at the C-terminal tail.

MATERIALS AND METHODS

SARS CoV E Protein Constructs—Full-length SARS CoV E and a truncated version were used in this work. Full-length SARS-CoV E protein (E_{FL}) was cloned into pTBMalE plasmid downstream of the MBP fusion tag and tobacco etch virus cleavage sequence. The plasmid was transformed into *Escherichia coli* strain BL21(DE3) codon plus for protein expression. The truncated form, E_{TR}, was cloned into pNIC28-Bsa4 with an N-terminal His_6 tag followed by a tobacco etch virus cleavage sequence. The plasmid was transformed into *E. coli* strain BL21(DE3) Rosetta T1R for protein expression. In both constructs, all three native cysteines (Cys-40, Cys-43, and Cys-44) were mutated into alanines. In addition, two E_{FL} mutants previously described by Cohen *et al.* (43) were prepared by site-directed mutagenesis: (i) P54A (E_{P54A}) and (ii) V56A/Y57A/V58A/Y59A (E_{4ALA}).

Protein Expression and Purification—Non-labeled E protein was produced by growing the culture in Terrific broth medium at 37 °C until the culture density reached an A_{600} of 2. Protein expression was induced by adding 0.5 mM isopropyl 1-thio-β-D-galactopyranoside and growing the culture overnight at 18 °C. The cells were harvested by centrifugation at 7,500 × *g* and stored at −80 °C.

Stable isotope-labeled E protein was produced by growing the culture in LB medium at 37 °C. When the culture density reached an A_{600} of 0.7, the medium was exchanged to M9 minimal medium at 25% of the initial volume to achieve a high density culture, as described previously (50). The M9 medium was appropriately supplemented with ^{15}N-NH_4Cl and [^{13}C]glucose (Cambridge Isotope Laboratories) to produce ^{15}N-labeled and $^{15}N/^{13}C$-labeled protein. Cultures were further grown for 1 h before inducing protein expression with 0.5 mM isopropyl 1-thio-β-D-galactopyranoside at 18 °C. After 6 h, cells were harvested as described above and stored at −80 °C.

Frozen cell pellets were resuspended in lysis buffer (20 mM Tris, pH 8.0, 300 mM NaCl, 5 mM imidazole, 2 mM β-mercaptoethanol, and 10% glycerol) supplemented with 1 mM PMSF and 1.5% Triton X-100. The cells were completely lysed by sonication and microfluidization. Insoluble particles were removed by centrifugation at 40,000 × *g*, and the supernatant was applied onto a pre-equilibrated nickel-nitrilotriacetic acid resin (Bio-Rad Profinity IMAC Ni^{2+}-charged). The resin was washed with 20 mM Tris, pH 8.0, 300 mM NaCl, 20 mM imidazole, 2 mM β-mercaptoethanol, and 10% glycerol. Bound peptide was eluted in 20 mM Tris, pH 8.0, 300 mM NaCl, 250 mM imidazole, 2 mM β-mercaptoethanol, 10% glycerol, and 5 mM myristyl sulfobetaine (C14SB). E_{TR} protein was directly TCA-precipitated and lyophilized, whereas E_{FL} was subjected to tobacco etch virus protease cleavage for 3 h at 30 °C prior to precipitation and lyophilization. Further purification was achieved by using reversed-phase HPLC on a Phenomenex Jupiter C4 semi-preparative column (250 × 10 mm, 300-Å pore size, 5-μm particle size). Lyophilized peptide was dissolved with 1% TFA in acetonitrile and separated under an isopropyl alcohol-acetonitrile linear gradient (4:1 (v/v) with 0.1% TFA). The identity and purity of peptide fractions were confirmed by SDS-PAGE and MALDI-TOF MS.

Gel Electrophoresis—Standard SDS-PAGE was performed in 13.5% Tris-glycine gel with TGS running buffer and stained with Coomassie Blue G-250. SDS-NuPAGE was performed in 4–12% NuPAGE® BisTris gel (Invitrogen) with NuPAGE® MES SDS running buffer and stained with SimplyBlue™ SafeStain (Invitrogen) according to the manufacturer's protocol.

To perform electrophoresis in the presence of perfluorooctanoic acid (PFO) detergent, we modified Invitrogen's SDS-NuPAGE protocol by replacing SDS with PFO. Lyophilized peptide was dissolved in sample buffer containing 4% PFO and heated at 65 °C for 5 min prior to loading. The gel was run at 80 V for 2–3 h with MES running buffer containing 0.5% PFO.

Blue native PAGE was performed as described previously (51). Lyophilized peptide was solubilized (0.1 mM) in sample buffer containing 25 mM SDS and either 25, 50, or 100 mM DPC. Aquaporin Z in 20 mM SDS (heated at 65 °C for 10 min) was included as an additional molecular weight marker.

Fourier Transform Infrared Spectroscopy—Sample preparation, data collection, and H/D exchange were performed essentially as described (32) on a Nicolet Nexus spectrometer (Madison, WI). The peptides were incorporated in multilamellar liposomes by dissolving a dry mixture of 1,2-dimyristoyl-*sn*-glycero-3-phosphate (DMPC; Avanti Polar Lipids) and lyophilized peptide in HFIP at a 50:1 molar ratio. Fourier self-deconvolution was performed for some spectra using the following parameters: full width at half height, 20 cm^{-1}; narrowing factor, $k = 1.5$) (52).

Analytical Ultracentrifugation—Sedimentation equilibrium experiments were performed using a Beckman XL-I analytical ultracentrifuge at 20 °C (53) and monitored by measuring the

absorbance at 280 nm. Lyophilized E_{TR} peptides were dissolved at A_{280} of 0.3, 0.5, and 0.8 (12-mm path length cell) in 20 mM sodium phosphate, pH 5.5; 50 mM NaCl; and for detergent either 5 mM C14SB, 100 mM DPC, or 12.5, 25, or 50 mM SDS. To match the density of the SDS-DPC mixture, D_2O was added at 61.6, 65, and 72.4%, respectively, to each SDS concentration. The samples were centrifuged in six-channel charcoal-filled Epon centerpieces using quartz windows. A radial distribution profile was acquired after sufficient time to reach equilibrium, as tested by HeteroAnalysis. The data were processed and fitted to several monomer/*n*-mer models in SEDFIT and SEDPHAT (54).

Circular Dichroism—CD data were acquired on a Chirascan CD spectrometer (Applied Photophysics) using a 0.2-mm quartz cuvette (Hellma). E_{TR} peptide samples were dissolved at 1 mg/ml in 20 mM sodium phosphate, 50 mM NaCl, pH 5.5, 100 mM DPC, with or without 50 mM SDS. CD spectra were acquired from 180 to 260 nm with a 1-nm spectral bandwidth and 3 replicates/spectra. Data points with excessive absorbance were excluded. After baseline subtraction, the data were analyzed in Dichroweb (55) by using the CDSSTR method (56) and the SMP180 reference set (57).

NMR Sample Preparation—Approximately 1.2 mg of lyophilized E_{TR} protein was solubilized in 100 μl of methanol and dried under a dry stream of N_2 gas, resulting in a thin protein film deposit. The tube was placed in a vacuum lyophilizer overnight to remove any residual methanol. The thin protein film was then solubilized with sample buffer containing 20 mM sodium phosphate, pH 5.5, 50 mM NaCl, and 50 mM SDS. The sample was vortexed and sonicated several times until a clear solution was obtained, indicating protein reconstitution into detergent micelles.

For paramagnetic relaxation enhancement (PRE) experiments, a single point mutation (S60C) was introduced into E_{TR} by site-directed mutagenesis using appropriate sets of primers. Expression and purification protocol of the E_{TR}-S60C mutant was the same as that of E_{TR} protein. For labeling, 0.3 mM ^{15}N-labeled E_{TR}-S60C was dissolved in 20 mM sodium phosphate, 50 mM NaCl, 200 mM SDS, and 0.8 mM DTT at pH 5.5 and split into two equal portions for parallel labeling with (1-oxyl-2,2,5,5-tetramethyl-Δ^3-pyrroline-3-methyl) methanethiosulfonate (MTSSL) (TorontoResearch Chemicals Inc.) and a diamagnetic analog of MTSSL: (1-acetyl-2,2,5,5-tetramethyl-Δ^3-pyrroline-3-methyl) methanethiosulfonate (dMTSSL; Toronto Research Chemicals Inc.). A 10-fold molar excess of both reagents was added from 75 mM stocks in methanol. The sample was vortexed for 30 min at high speed and incubated overnight at room temperature. A centrifugal filter unit (10,000 molecular weight cut-off; Millipore Corp.) was used to remove excess of both reagents. Labeled samples were washed four times by concentrating to 100 μl. After a fourth wash, the sample was concentrated to 180 μl for NMR measurements.

Partial alignment of the E_{TR} protein-micelle complexes relative to magnetic field was obtained by using stretched polyacrylamide hydrogels (58, 59). A 7% polyacrylamide gel was polymerized in a gel chamber of 5.4-mm inner diameter. After complete polymerization, gels were washed in H_2O overnight and then twice with sample buffer containing 20 mM sodium phosphate and 50 mM NaCl at pH 5.5. The gels were then completely dried at room temperature. The protein solution containing E_{TR}/SDS was soaked into the dried gels over 2 days to ensure complete rehydration. The hydrated 7% gel was then compressed into a 4.2-mm inner diameter open-ended tube using the gel press assembly (New Era Enterprise, Inc.).

NMR Spectroscopy—NMR experiments were performed at 308 K using an Avance-II 700 NMR spectrometer with cryogenic probe. Sodium 2,2-dimethyl-2-silapentane-5-sulfonate was used as the internal reference for ^{1}H nuclei. The chemical shifts of ^{13}C and ^{15}N nuclei were calculated from the ^{1}H chemical shifts. The NMR data were processed using TopSpin version 3.1 and analyzed using CARA. Sequence-specific assignment of backbone $^1H^N$, ^{15}N, $^{13}C'$, and $^{13}C^\alpha$ was achieved by using two-dimensional ^{1}H-^{15}N TROSY-HSQC, three-dimensional HNCO, HN(CA)CO, HNCA, HN(CO)CA, and HNCACB experiments on a ^{15}N/^{13}C-labeled E_{TR} protein. Side-chain resonances were assigned using three-dimensional ^{15}N-resolved NOESY-HSQC (80-, 100-, and 150-ms mixing time), (H)CCH-TOCSY, and ^{13}C-resolved NOESY-HSQC (120-ms mixing time). To identify membrane-embedded residues, the NMR sample was lyophilized overnight and reconstituted in 99% D_2O. Immediately after reconstitution, two-dimensional ^{1}H-^{15}N TROSY-HSQC was collected. For paramagnetic probe measurements, ^{15}N-HSQC spectra were recorded in the presence and absence of 1 mM dry 5-doxyl stearic acid (5-DSA) or 16-doxyl stearic acid (16-DSA). Axially symmetric alignment tensor coefficients (axiality and rhombicity) were calculated using MODULE (60). The PRE effect was measured using ^{15}N HSQC spectra of the S60C mutant before spin labeling and after MTSSL and dMTSSL labeling. The titration experiments with HMA, Nsp3a, or SH(45–65) were performed with ^{15}N-labeled E_{TR} in a 1:4 molar ratio of SDS/DPC micelles at 318 K. Chemical shift perturbation (CSP) values were calculated using the following formula.

$$\mathrm{CSP} = \sqrt{\Delta\delta H^2 + (0.23 \times \Delta\delta N)^2} \qquad \text{(Eq. 1)}$$

Structure Calculation—NOE distance restraints were obtained from ^{15}N NOESY-HSQC (mixing time 80, 100, and 150 ms) and ^{13}C NOESY-HSQC (mixing time 120 ms) spectra, respectively. Backbone dihedral angle restraints (φ and ψ) were derived from $^{13}C'$, $^{13}C^\alpha$, $^{13}C^\beta$, $^1H^\alpha$, and $^1H^\beta$ chemical shift values using TALOS+ (61). The short range and medium range NOE connectivities were used to establish the sequence-specific ^{1}H NMR assignment and to identify elements of the regular secondary structure. Hydrogen bonds were derived from the H/D exchange experiment and NOE connectivity.

Distance restraints were obtained from the measured PRE effect using the procedures described previously (62–64). The intensities of cross-peaks in the MTSSL (*Ip*) and dMTSSL (*Id*) were calculated in CARA. The correlation time was set to 10 ns. The ratios of intensities (*Ip*/*Id*) were normalized against a set of the eight highest *Ip*/*Id* ratios, which were assumed to belong to peaks unaffected by PRE. For peaks with ratios below 0.15, no lower distance restraints were used, whereas upper restraints were set to 15 Å. For peaks with ratios above 0.9, only upper restraints of 25 Å were utilized. For peaks with ratios between

0.15 and 0.9, upper and lower distance restraints were generated using ±3 Å margins.

Structure calculations were performed using CYANA version 3.0 (65, 66) and visualized using PyMOL (Schroedinger LLC, New York). CNS 1.3 (67, 68) was used to refine the structure using the standard simulated annealing protocol. All of the restraints used in the calculations to obtain a total of 15 structures and all of the structure statistics are summarized in Table 1.

Single Channel Activity Measurement—Ion channel activity of E_{TR} was measured by using Nanion Port-a-Patch®. Briefly, giant unilamellar vesicles of 1,2-diphytanoyl-*sn*-glycero-3-phosphocholine containing 10% cholesterol were prepared in 1 M sorbitol using Nanion Vesicle Prep Pro®, following the manufacturer's protocol. Into 100 μl of a giant unilamellar vesicle solution, 0.5 μl of E_{TR} peptide solution in ethanol (0.1 mg/ml) was added and incubated for 1 h at room temperature. E_{TR}-containing giant unilamellar vesicles were subsequently deposited onto 6–8 megaohm NPC®-1 chips (Nanion). Conductance was measured under symmetrical buffer conditions (10 mM HEPES, 500 mM NaCl, pH 5.5).

Surface Plasmon Resonance—The *nsp3a* sequence was subcloned from pcDNA3(+) into pET28b upstream of a C-terminal His_6 tag for expression in *E. coli*. The protein was expressed and purified as described previously by Serrano *et al.* (69). A negative control, consisting of C-terminal peptide from the small hydrophobic (SH) protein of human respiratory syncytial virus (RSV SH(45–65)), was synthesized by standard solid phase and purified by reverse-phase HPLC. Surface plasmon resonance measurements were performed on a Biacore 3000 system (GE Healthcare) using 10 mM phosphate buffer at pH 6.5, 100 mM NaCl, 3 mM EDTA, 0.05% *n*-octyl-β-D-glucopyranoside, and 0.27% C14-betaine at 25 °C. E_{TR} was immobilized to 15,000 RU onto a research grade CM5 sensor chip (GE Healthcare) using standard amine-coupling chemistry. Briefly, a buffer-equilibrated carboxymethyl dextran surface was activated with a 10-min injection of a 1:1 mixture of 0.05 M *N*-hydroxysuccinimide and 0.2 M *N*-ethyl-*N*-[3-(diethylamino)propyl]carbodiimide. E_{TR} peptides dissolved in 10 mM sodium acetate, 15 mM DPC (pH 5.0) were passed over the activated surface to achieve the desired response level. Another 10-min injection of 1 M ethanolamine-HCl (pH 8.5) was used to deactivate the surface and remove any non-covalently bound protein. Kinetic measurements of immobilized E_{TR} association with Nsp3a and SH(45–65) (49 nM to 25 μM in 10 2-fold serial dilutions) were performed with a 1-min association phase and 5-min dissociation phase at a 30 μl/min flow rate. Each concentration was tested in duplicate. No regeneration was necessary because all complexes dissociated within the monitored time. Sensorgrams were double-referenced (70) and globally fit to a steady-state model to obtain affinity values.

RESULTS AND DISCUSSION

Expression and Purification of SARS-CoV E Protein—Initially, we successfully expressed and purified full-length SARS-CoV E protein (E_{FL}, Fig. 1*B*) by using either a β-barrel (71) or MBP as fusion tags. However, the yield of pure protein was low due to the presence of truncations (not shown). Nevertheless, the pure sample obtained (Fig. 1, *C* and *D*) was sufficient for backbone assignment in SDS micelles, although not to produce a three-dimensional model. Therefore, a series of hexahistidine-tagged SARS-CoV E constructs were screened to obtain an expressing and well behaved sample. The best construct, encompassing residues 8–65, was successfully expressed in *E. coli* and purified by affinity chromatography in milligram amounts without any enzymatic cleavage steps. This truncated construct (E_{TR}; see Fig. 1*B*) has an N-terminal His tag and a 16-residue linker that connects it to residues 8–65. The purified peptide appeared in MALDI-TOF MS as a single-charged peak at 8,997 Da and a double-charged peak at 4,512 Da, consistent with the calculated molecular mass of E_{TR}, 8,995 Da, and a small proportion of larger (dimer to pentamer) oligomers (Fig. 1*E*). After HPLC, the E_{TR} monomer (9 kDa) showed anomalous migration in standard SDS-PAGE (Fig. 1*F*), as reported previously for the full-length protein (31).

Identification of the Membrane-embedded Region of E_{TR} by NMR—Screening of reconstitution conditions identified SDS as the best environment to achieve good peak dispersion in both dimensions (Fig. 2*A*). Comparison of ^{1}H-^{15}N TROSY-HSQC spectra in water and in 99% D_2O (Fig. 2, *A* and *B*) identified a stretch of 21 residues, from Leu-18 to Leu-39, protected from H/D exchange. The same residues were protected from H/D exchange in E_{FL} (not shown), which indicates that both E_{TR} and E_{FL} have only one TM domain.

The topology of E_{TR} was also delineated by introducing the paramagnetic probes 5-DSA and 16-DSA. Upon the addition of 5-DSA, a slight intensity reduction was observed around residues 11–20 and 40–55 (Fig. 2*C*), suggesting that these residues are located at or near the micelle surface. The addition of 16-DSA caused pronounced intensity reduction in the stretch of TM residues 19–40 and periodically in the stretch 48–61 (Fig. 2*D*). Together with the H/D exchange data (Fig. 2, *A* and *B*), these results again demonstrate the presence of a single TM domain and suggest that the stretch of residues 55–65 corresponds to a domain bound to the surface of the micelle. Finally, a ^{1}H-^{15}N steady-state heteronuclear NOE experiment (Fig. 2*E*) showed that the protein forms a well folded structure, with high $^{1}H/^{15}N$ NOE values. However, more dynamic regions (lower $^{1}H/^{15}N$ NOE values) can be observed (i) at the N terminus and (ii) at residues 46–55, which connects the TM domain to the proposed membrane-bound domain. The latter is predicted to be α-helical (Fig. 2*F*).

NMR Structure Determination of E_{TR} in SDS Micelles; Structure Calculation—The restraints shown in Table 1 were used in a calculation to obtain a total of 15 structures, with a root mean square deviation of 0.27 ± 0.11 and 0.70 ± 0.13 Å for backbone and all heavy atoms, respectively (Fig. 3*A*). A longer α-helix (residues 15–45) encompasses the TM domain, which is connected to another shorter C-terminal α-helix (residues 55–65) by a flexible (see Fig. 2*E*) linker domain (residues 46–54), forming an L-shape. The short extramembrane helix may be partially bound to the micelle surface, as suggested by the pattern of intensity attenuation of paramagnetic reagents (see Fig. 2, *B* and *C*). The most affected residues, which would face the micelle surface, are Val-52, Thr-55, Tyr-59, and Lys-63 (Fig. 3*B*).

The TM α-helix has a slight bend at residues 26–30, consistent with previous results obtained for the synthetic TM

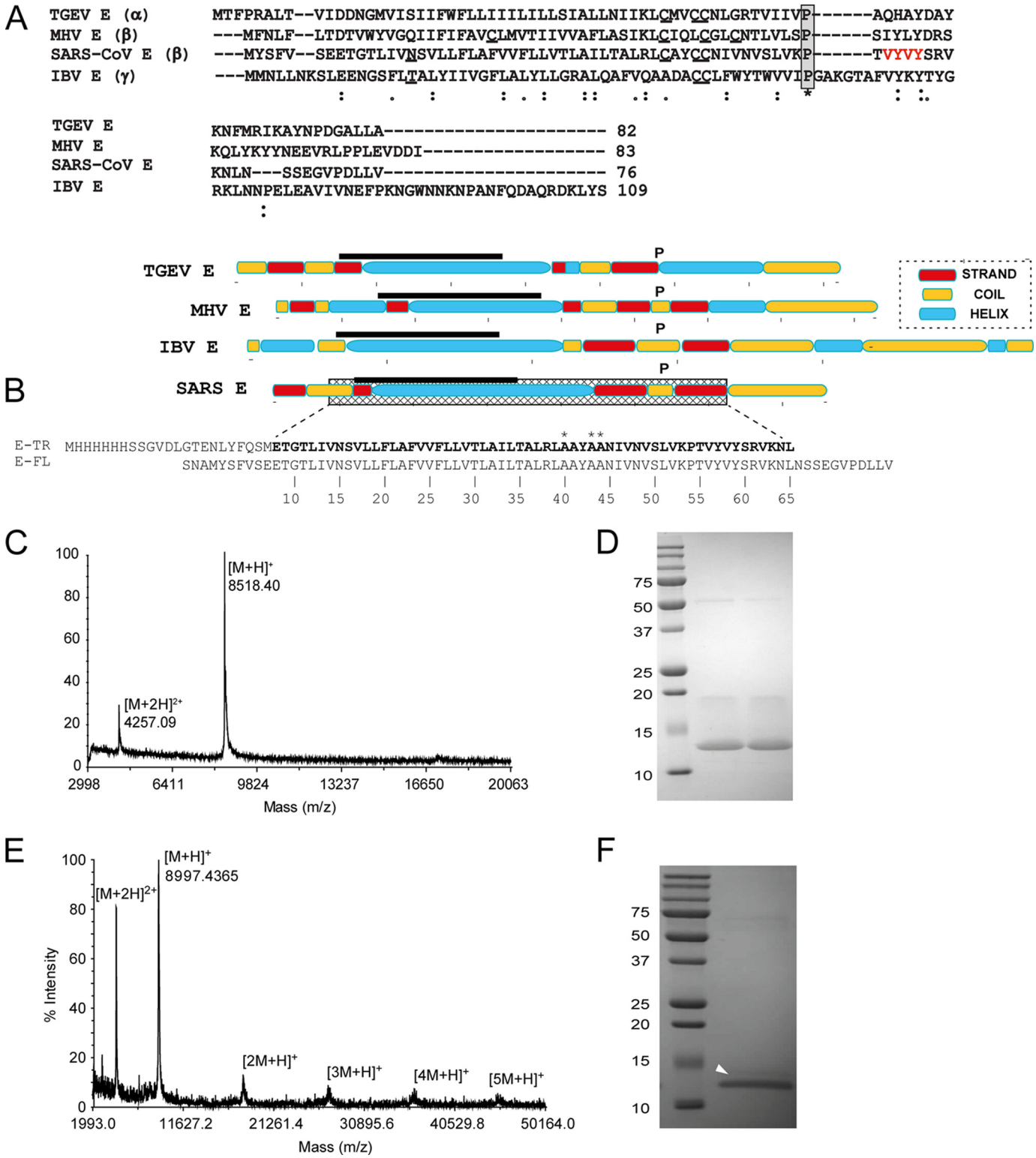

FIGURE 1. **Sequences, expression, and purification of SARS-CoV E_{TR}.** *A*, alignment of representative sequences of E proteins in α-, β-, and γ-coronaviruses. The cysteine residues are *underlined*, the conserved proline is *highlighted* (*gray*), and the four residues mutated to alanine in the E_{4ALA} mutant (see "Materials and Methods") are shown in *red*. For these four proteins, the prediction of secondary structure is shown *below* in a *color code*, with the TM domain indicated as a *black line*; *B*, proteins used in the present work: a His-tagged construct (E_{TR}) encompassing residues 8–65 (*boldface type*, *underlined*), and full-length SARS-CoV E (E_{FL}). In E_{FL}, the fragment SNA results from the cleavage of the tag. In both proteins, the native cysteines were mutated to alanine (C40A, C43A, and C44A; see *asterisks*); *C* and *D*, MALDI-TOF MS spectra (*C*) and standard SDS-PAGE (*D*) of pure E_{FL} with the species labeled; *E* and *F*, same as for purified E_{TR}; the identities of various single- and double-charged species are indicated. The calculated mass of E_{TR} is 8,995 Da.

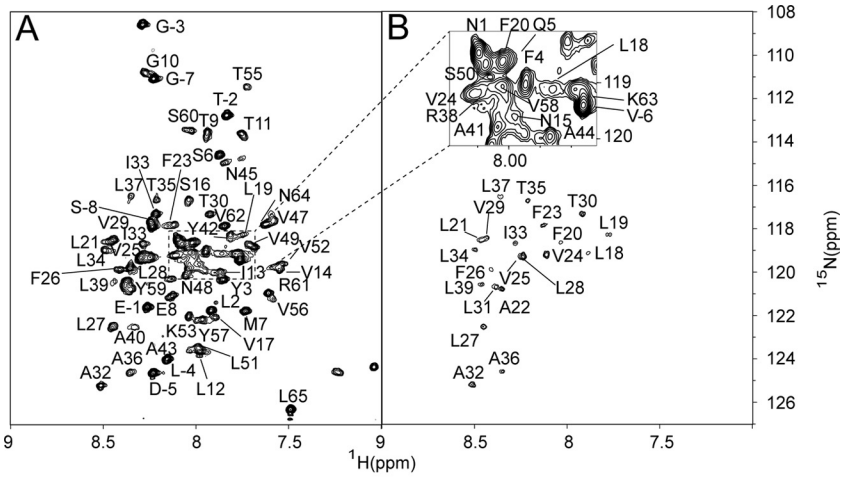

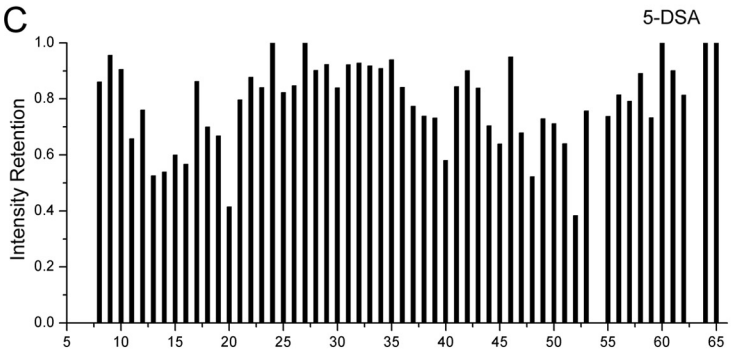

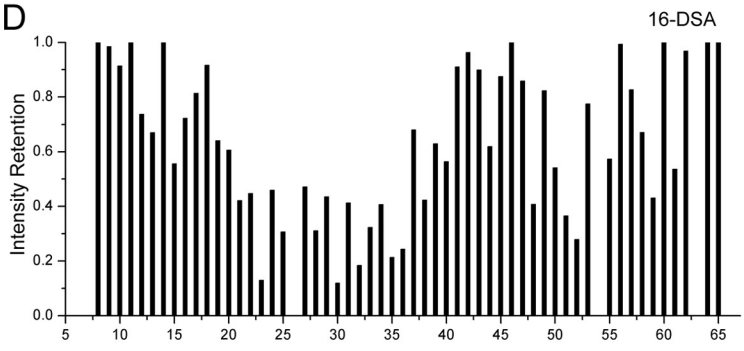

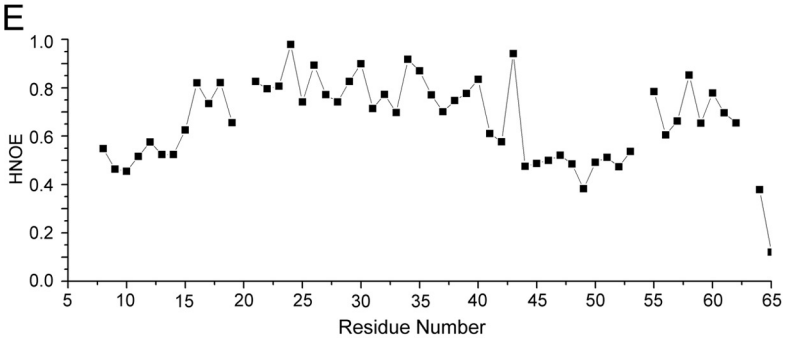

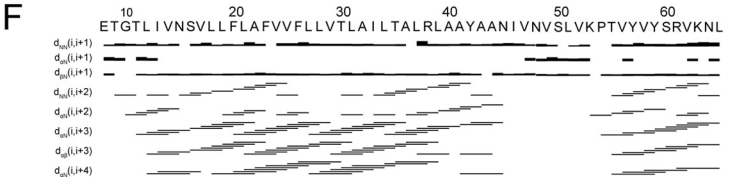

TABLE 1
Restraints and structure statistics for the selected 15 structures of E_{TR}

NMR restraints	
Total unambiguous distance restraints	2,258
Intraresidual	1,334
Sequential ($\|i-j\|=1$)	230
Short-range ($\|i-j\|\leq 1$)	1,564
Medium ($2\leq\|i-j\|\leq 4$)	321
Long range ($\|i-j\|\geq 5$)	11
Dihedral angle restraints	85
Hydrogen bond restraints[a]	20
RDC restraints	44
PRE restraints	38
Root mean square deviation from the experimental residual dipolar couplings (Hz)	
$^1D_{NH}$	0.71 ± 0.03
Root mean square deviation from the average atomic coordinates (residues 12–63, Å)[b]	
Backbone atoms	0.27 ± 0.11
All heavy atoms	0.70 ± 0.13
Ramachandran analysis (%)	
Residues in most favored regions	87.5
Residues in additional allowed regions	12.5
Residues in generously allowed regions	0.0
Residues in disallowed regions	0.0

[a] Backbone hydrogen bonds of α-helix were applied to regions confirmed to be α-helical, according to the local NOE pattern and H^N-H_2O chemical exchange experiments.
[b] Statistics were calculated and averaged over an ensemble of 15 structures with lowest target function according to CYANA.

domain in DPC micelles (34). A kink near this location is suggested by the short distance (2.0 ± 0.1 Å) between Thr-30 Hγ and the carbonyl oxygen at Phe-26, in the range of a hydrogen bond (Fig. 3*C*).

Effect of Truncation and Environment on E_{TR} Secondary Structure—To assess the effect of the truncation and the presence of a His tag on the E_{TR} secondary structure, E_{TR} and E_{FL} were compared. The possible effect of the reconstitution environment was also determined.

CD and IR Spectra of E_{TR} and E_{FL} in Detergent and Lipid Membranes—The CD spectra of E_{TR} in DPC, SDS, and mixed (1:2 molar ratio) SDS/DPC micelles are almost superimposable (Fig. 4*A*) with minima at 209 and 222 nm. Also, these data are entirely consistent with the CD spectra of E_{FL}, which was predominantly α-helical in both SDS and DPC micelles (71). When reconstituted in DMPC membranes, E_{TR} and E_{FL} produced an almost identical spectrum, with an amide I band centered at 1,655 cm^{-1} (Fig. 4*B*) characteristic of a predominantly α-helical conformation. Overall, these data show that both E_{TR} and E_{FL} (i) are predominantly α-helical and (ii) have a secondary structure that is not significantly affected by the reconstitution environment, supporting the relevance of the E_{TR} structure (Fig. 3).

^{13}Cα Chemical Shifts—^{13}Cα chemical shifts are highly correlated with secondary structure (72, 73). Comparison of ^{13}Cα chemical shifts of E_{TR} and E_{FL} in SDS (Fig. 4*C*) shows that E_{TR} shifts (*red*) are almost identical to their counterpart residues (residues 8–65) in E_{FL} (*blue*). In E_{FL}, the shifts for the last 10 residues (residues 66–76) are predicted to correspond to random coil, which is consistent with results obtained previously with a synthetic peptide spanning residues 59–76 (39). This peptide produced a broad amide I band in the IR spectrum centered around 1,650 cm^{-1} and immediately experienced complete H/D exchange.

When the ^{13}C shifts for E_{TR} were compared for SDS and an SDS/DPC mixture (1:4 molar ratio), only the N-terminal region (residues 7–15) showed minor differences. Finally, a comparison between E_{FL} and E_{TR} in an SDS/DPC mixture (1:4 molar ratio) also revealed an almost identical pattern in the C-terminal tail (not shown), although the spectral resolution for E_{FL} was reduced in other regions. Overall, these results are consistent with those shown above (Fig. 4, *A* and *B*), indicating that the detergent used, the tag, and the truncation has a minimal on E_{TR} secondary structure.

Ion Channel Activity of E_{TR} and Its Inhibition by HMA—Purified E_{FL} has channel activity (71), which is inhibited by the drug HMA (30). An *I*/V plot obtained in a symmetrical 0.5 M NaCl experiment for purified E_{TR} in 1,2-diphytanoyl-*sn*-glycero-3-phosphocholine (Fig. 5*A*) was used to determine a conductance of 0.39 ± 0.02 nanosiemens. For comparison, synthetic full-length SARS-CoV E and E_{TM} (residues 7–38) produced single channel conductances of 0.19 ± 0.06 picosiemens and 0.18 ± 0.12 nanosiemens in 1 M NaCl (35), although the values were higher in 1 M KCl, with 0.37 ± 0.16 and 0.31 ± 0.12 for full-length SARS-CoV E and E_{TM}, respectively. The lower conductance observed in synthetic samples may be due to extraneous modifications or impurities resulting from exposure to harsh chemicals. Representative traces of E_{TR} channel activity (Fig. 5*B*) and complete inhibition after the addition of 10 μM HMA (Fig. 5*C*) suggest that E_{TR} is entirely functional.

To determine the binding site for HMA, we measured the differences in CSP values before and after the addition of the drug (Fig. 5, *D* and *E*). In SDS, the average CSP value was low, 0.006 ppm (Fig. 5*F*), even at an HMA/E_{TR} 10:1 molar ratio, suggesting no significant binding. However, the same panel shows that the addition of HMA to E_{TR} in mixed SDS/DPC (1:4 molar ratio) micelles produced an average CSP value of 0.013 ppm, even at an HMA/E_{TR} 2:1 molar ratio.

Except for Asn-64 and Leu-65, the residues that showed significant CSP (CSP ≥ 0.025 ppm) clustered near the membrane interface regions of the TM domain (Fig. 5*F*, see *arrows*). Near the N-terminal side of the TM domain, the most affected were Glu-8, Gly-10, Thr-11, Val-14, Asn-15, and Ser-16, the latter two consistent with observations made on the TM channel in DPC (34). At the C-terminal end of the TM, Leu-37 was the most affected, suggesting that the interaction of HMA at Hε of Arg-38 reported previously (34) may have been an artifact due to the use of a TM peptide.

Oligomeric State of E_{TR}

Gel Electrophoresis—The localized changes in chemical shifts observed after HMA addition to E_{TR} in mixed DPC/SDS micelles (Fig. 5*E*), but not in SDS micelles (Fig. 5*D*), suggest that binding sites for HMA may have been induced after DPC addi-

FIGURE 2. **Topology and secondary structure of E_{TR}.** ^{1}H-^{15}N TROSY-HSQC spectra of 0.2 mM E_{TR} in 50 mM SDS in H_2O (*A*) and in 99% D_2O (*B*). The cross-peaks are labeled by *one-letter code* and *residue number*; *C* and *D*, peak intensity reduction upon the addition of 5-DSA (*C*) and 16-DSA (*D*), calculated as the ratio of peak intensity before and after the addition of the paramagnetic reagents; *E*, ^{1}H-^{15}N steady-state heteronuclear NOE experiment; *F*, sequential and medium-ranged NOE connectivity between residues, displayed as bands *under* the respective residues.

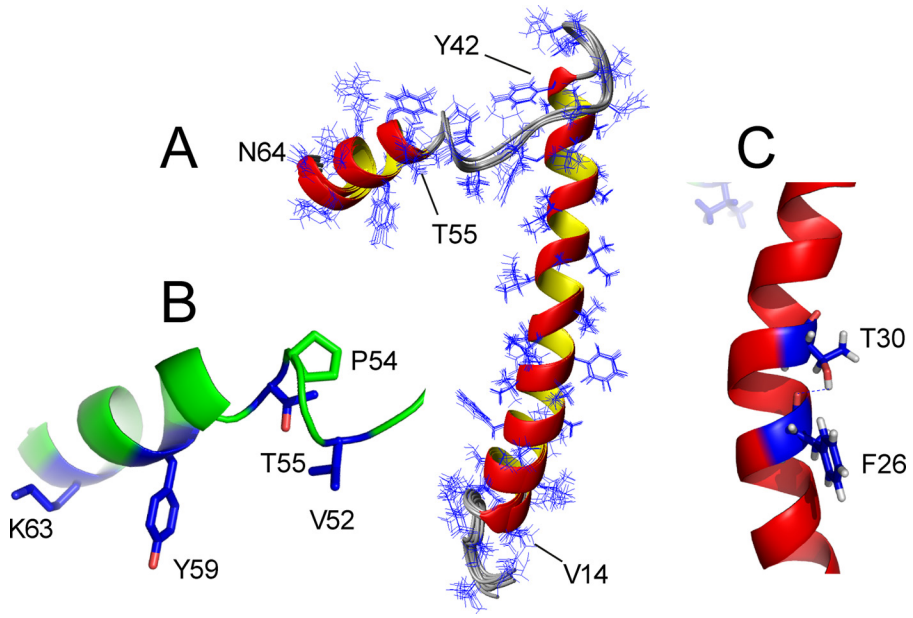

FIGURE 3. **Structural model of E_{TR}.** *A*, superposition of an ensemble of 15 calculated simulated annealing structures of E_{TR} (only the sequence corresponding to E protein, 8–65, is shown). Side chains are shown as *line representations*; the residues at the ends of the two helical segments are indicated. *B*, residues of the C-terminal extramembrane α-helix oriented toward the micelle surface (*blue*). *C*, *ribbon representation* of the TM central region, with the carbonyl oxygen of Phe-26 forming a hydrogen bond to the side chain of Thr-30.

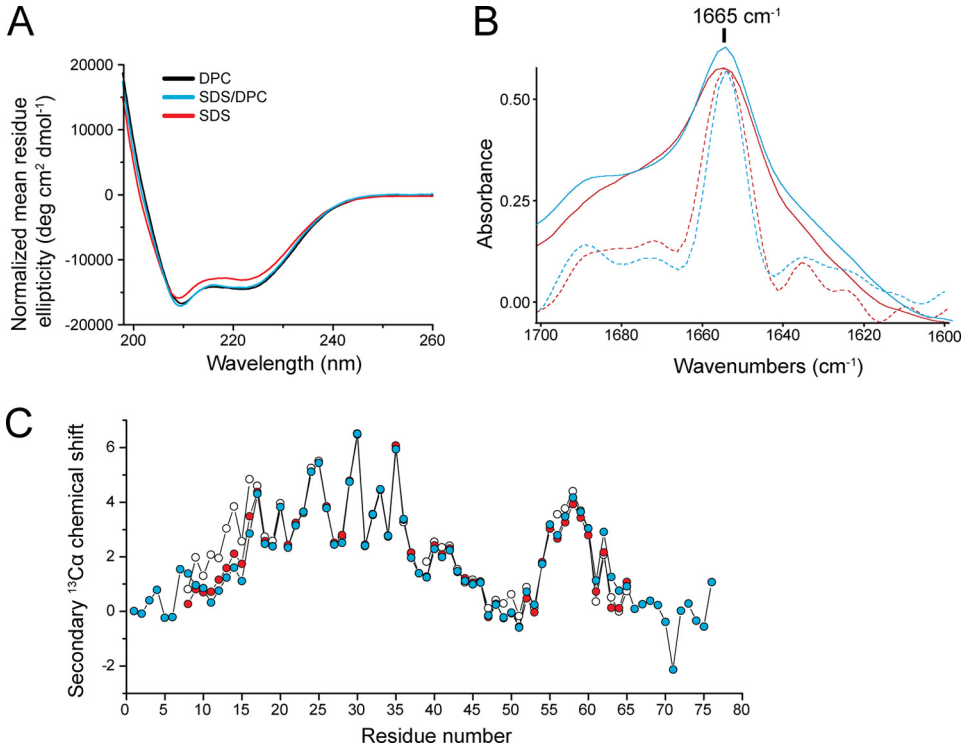

FIGURE 4. **Equivalence in secondary structure of E_{TR} and E_{FL}.** *A*, CD spectra of E_{TR} in DPC (*black*), 1:2 molar ratio SDS/DPC mixture (*blue*), and SDS (*red*). *B*, infrared amide I band of E_{TR} (*red*) and E_{FL} (*blue*) in DMPC lipid bilayers and their respective Fourier self-deconvolved spectra (*dotted lines*). *C*, comparison of secondary $^{13}C\alpha$ chemical shifts (deviation from tabulated random coil $^{13}C\alpha$ chemical shift values) for E_{TR} (*red dots*) and E_{FL} (*blue dots*) in SDS micelles and for E_{TR} in (1:4 molar ratio) mixed SDS/DPC micelles (*white dots*). For the latter, Pro-54 and Thr-55 were excluded from the analysis due to significant line broadening; Arg-38 was excluded from the analysis due to the peak overlapping.

tion to SDS, possibly through E_{TR} increased oligomerization and population of the pentameric form. Thus, we examined the oligomeric state of E_{TR} using gel electrophoresis performed in the presence of SDS or an SDS/DPC mixture. In contrast with the results obtained in normal SDS-PAGE (Fig. 1), we used NuPAGE, where E_{TR} migrated with its expected monomer molecular weight, as a single band at 9 kDa (Fig. 6*A*). No oligomerization is consistent with the lack of interaction between HMA and E_{TR} observed in SDS micelles.

To test the effect of DPC, in a blue native polyacrylamide gel, a constant SDS concentration (25 mM) was titrated with increasing DPC (Fig. 6*B*), from 1:1 to a 1:4 molar ratio. Bands

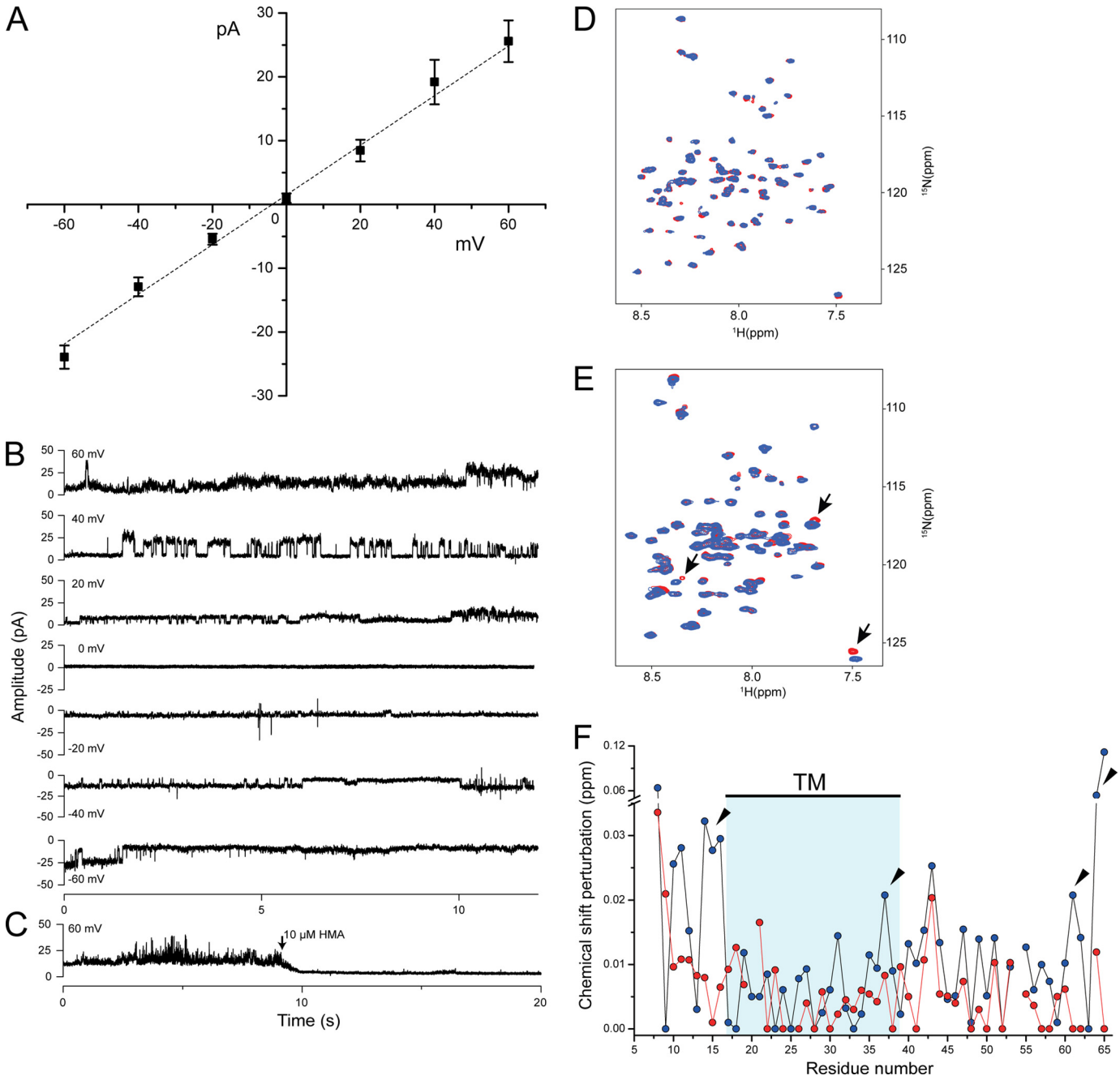

FIGURE 5. **Channel activity of E_{TR} and interaction with HMA.** *A*, *I*/*V* plot for E_{TR} in 1,2-diphytanoyl-*sn*-glycero-3-phosphocholine bilayers in a symmetrical experiment where both cis and trans compartments contained 10 mM HEPES and 500 mM NaCl at pH 5.5. Each *point* represents the mean of at least three current readings. The *line* is a linear regression fit of data points, which produced a slope of 0.39 ± 0.02 nanosiemens. *B*, selected traces of 12 s each, recorded at various holding potentials of E_{TR}. *C*, channel activity recorded at 60 mV holding potential and after the addition of 10 μM HMA (*arrow*). *D*, ^{1}H-^{15}N TROSY-HSQC spectra of 0.1 mM ^{15}N-labeled E_{TR} in SDS micelles (*D*) before (*blue*) and after (*red*) the addition of 1 mM HMA. *E*, same as for 0.2 mM ^{15}N-labeled E_{TR} in (1:4 molar ratio) SDS/DPC micelles upon titration with 0.4 mM HMA. Some shifts are indicated with *arrows*; *F*, CSP of the backbone amide resonances of E_{TR} before and after the addition of HMA in SDS (*red*) and (1:4 molar ratio) SDS/DPC micelles (*blue*). Note that the HMA/E_{TR} molar ratio was 10 in SDS and only 2 in SDS/DPC micelles. The *arrows* show residues with significant change in chemical shifts after the addition of HMA. The TM domain is indicated only to guide the eye.

consistent with dimers and trimers were observed at 1:1 and 1:2 molar ratios, whereas tetramers and pentamers were observed at a 1:4 molar ratio. This increasing oligomerization is again consistent with the binding of HMA observed in the presence of DPC.

Sedimentation Equilibrium, SDS/DPC Micelles—For a sample corresponding to a 1:4 molar ratio of SDS/DPC, the equilibrium sedimentation data (Fig. 7*A*) could be fitted to several oligomeric models, from trimers to heptamers (Fig. 7*B*). Similar ambiguous results were obtained for a 1:2 molar ratio SDS/DPC mixture (Fig. 7*C*), suggesting that E_{TR} forms a mixture of oligomers in SDS/DPC micelles, consistent with electrophoresis results (Fig. 6). The fit of the traces (Fig. 7*A*) to a monomer-pentamer model produced an apparent K_a of 1.25×10^{15} M^{-4} (*i.e.* 6×10^{3} M^{-1}) or a K_d for monomer-monomer interaction of 0.17 mM and a molar fraction standard free energy change (74),

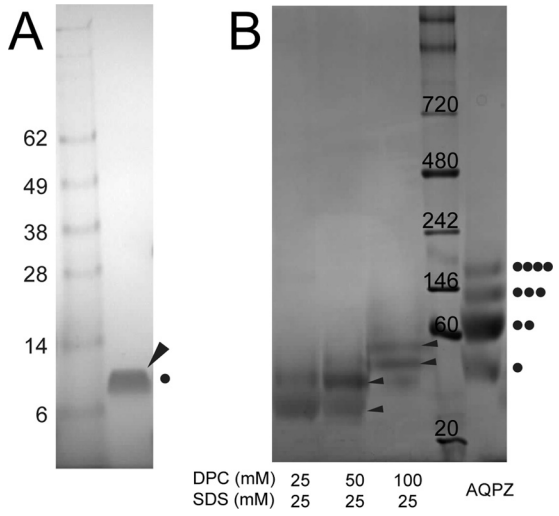

FIGURE 6. **Gel electrophoresis of E_{TR} in SDS and in a SDS/DPC mixture.** Shown are E_{TR} in 4–12% SDS-NuPAGE (*A*) and 4–16% blue native PAGE (*B*) of E_{TR} in 25 mM SDS with increasing concentration of DPC, as indicated. *E. coli* aquaporin Z (*AQPZ*) was included as an additional molecular weight marker. Bands and oligomeric states are indicated by *arrows* and *black dots*, respectively.

ΔG_x^0, of approximately −4 kcal·mol^{-1}. Overall, the above results show that higher oligomeric states, including pentamers, are observed when increasing the DPC concentration, consistent with the larger shifts observed after adding HMA to mixed DPC/SDS micelles.

E_{TR} Forms Pentamers in C14 Betaine and PFO—We have shown previously that SARS-CoV E TM domain and E_{FL} form pentamers (36, 71). When E_{TR} was solubilized in C14 betaine detergent (Fig. 7*D*), data could be optimally fitted to a monomer-pentamer model ($K_a = 10^{16}$ M^{-4}) with a significantly lower χ^2 than that obtained in SDS/DPC. Also, the mobility of E_{TR} in PFO-NuPAGE (Fig. 7*E*) corresponds to a molecular mass of 45 kDa (*i.e.* a pentameric form). Thus, E-TM, E_{TR}, and E_{FL} show a similar oligomerization behavior, being able to form pentameric channels that are inhibited by HMA.

Interaction of E_{TR} with Nsp3a—The interaction of Nsp3 with SARS-CoV E protein, thought to be related to E ubiquitination, was previously mapped to an N-terminal acidic domain, Nsp3a (49). Although the site of interaction with E is not known, it is likely to involve the C-terminal tail because it is the largest extramembrane domain. Thus, to test that the conformation of

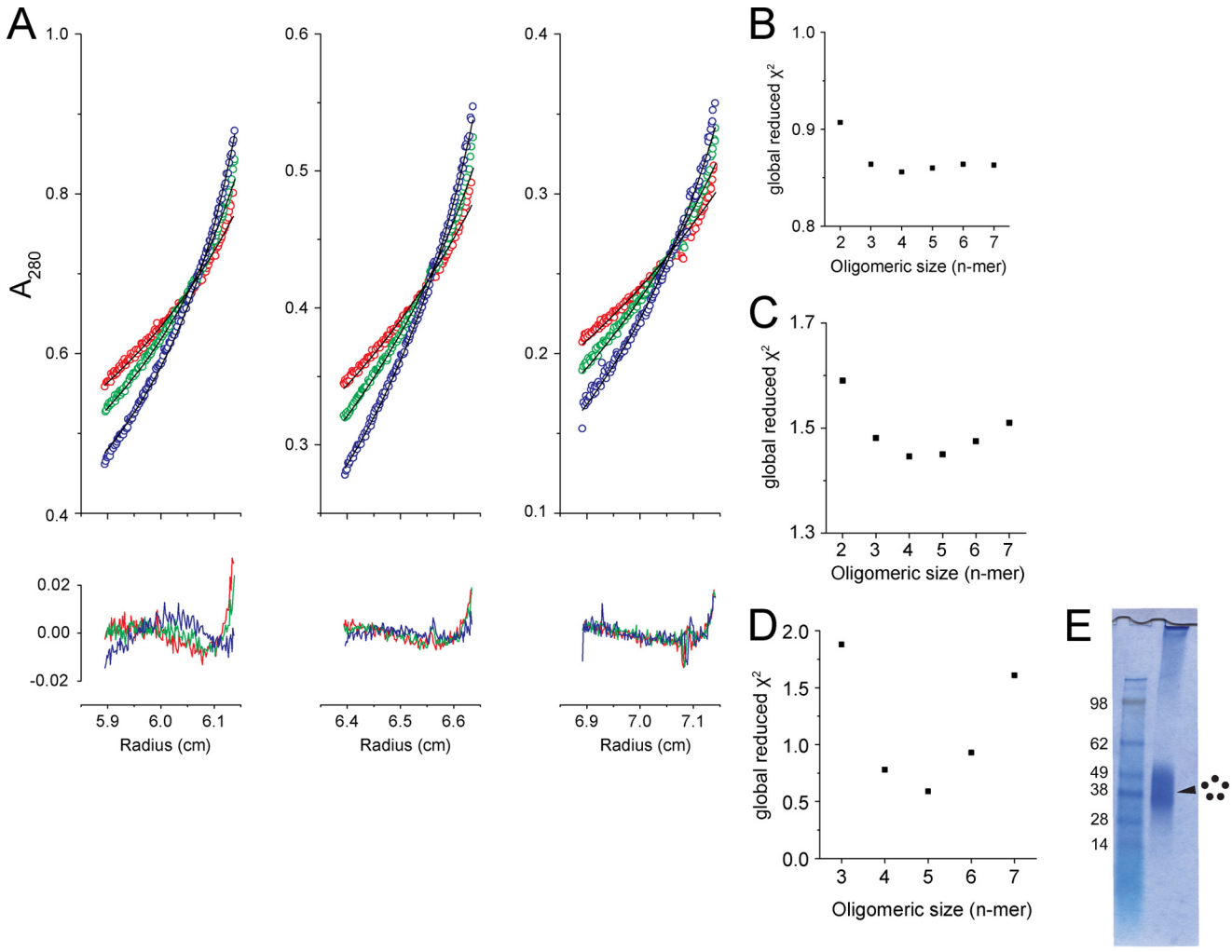

FIGURE 7. **Sedimentation equilibrium of E_{TR} in SDS/DPC micelles.** *A*, radial distribution profiles (*open circles*) of E_{TR} in a (25:100 mM) SDS/DPC mixture at 16,600 rpm (*red*), 20,300 rpm (*green*), and 24,900 rpm (*blue*). The profile was fitted to a monomer-pentamer self-association model (*black line*), and the fitting residuals are shown *below* each plot. *B–D*, global reduced χ^2 values obtained after data fits to different monomer/*n*-mer models of E_{TR} association in SDS/DPC micelles (*B*), a 50:100 mM SDS/DPC mixture (*C*), and 5 mM C14-betaine (*D*). *E*, 4–12% PFO-NuPAGE of E_{TR}.

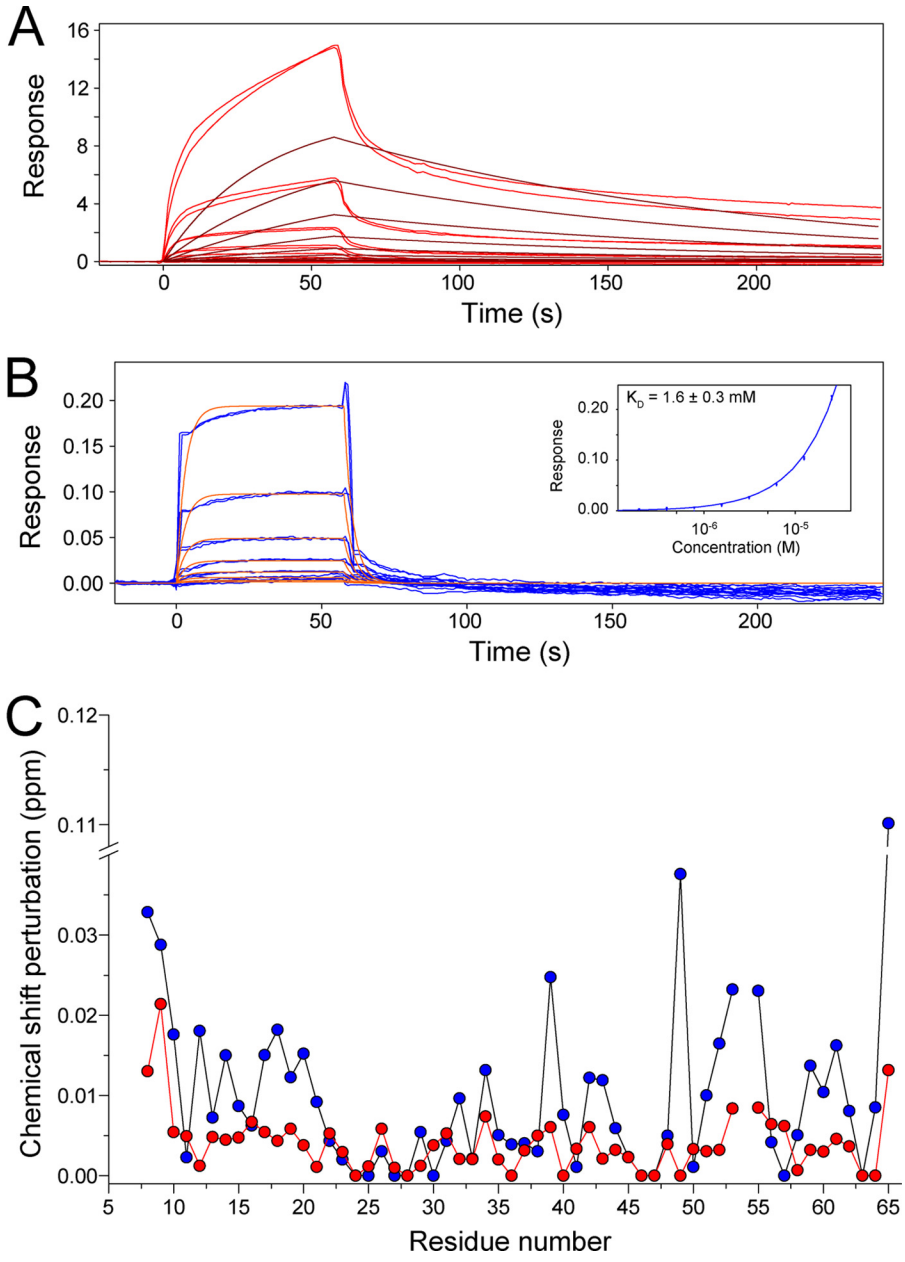

FIGURE 8. **Interaction between E_{TR} and Nsp3a.** *A*, sensorgrams corresponding to the interaction between purified RSV SH(45–65) and immobilized E_{TR} (*red*). The steady-state model (*dark red*) did not produce a good fit to a 1:1 model of interaction. The association phase extends from 0 to 60 s, whereas the dissociation phase extends for minutes. *B*, same as for Nsp3a and immobilized E_{TR} (*blue*) and fit to a steady-state model (*red*). *Inset*, dose-response plot, where the equilibrium responses of Nsp3a were plotted against the $\log_{10}$(concentration) of Nsp3a. Although the fit (*blue line*) yields an affinity of 1.6 mM, binding is already evident even in the interval 1–10 μM Nsp3a concentration. *C*, CSP of the backbone amide resonances of 0.2 mM ^{15}N-labeled E_{TR} in (1:4 molar ratio) SDS/DPC micelles upon titration with 0.4 mM Nsp3a (*blue dots*) or the negative control RSV SH(45–65) (*red dots*).

E_{TR} is structurally equivalent to the corresponding sequence in E_{FL}, we tested its ability to interact with Nsp3a (49) using surface plasmon resonance.

As a negative control, the mock peptide RSV SH(45–65) (see "Materials and Methods") was used to bind to immobilized E_{TR} in detergent (see "Materials and Methods") (Fig. 8*A*). Binding and unbinding of RSV SH(45–65) was very slow (>1 min), and the data could not be fitted to any model, suggesting a nonspecific interaction.

In contrast, rapid and reversible interaction was observed using purified Nsp3a (Fig. 8*B*). These data could be fitted with a stoichiometry of 1:1, although the end point could only be estimated. From that model, affinity was determined as 1.6 mM, although we note that binding is already evident at concentrations as small as 1–10 μM (see Fig. 8*B*, *inset*).

The residues involved in the interaction between Nsp3a and E_{TR} were identified by the differences in CSP values before and after the addition of Nsp3a to E_{TR} in SDS/DPC micelles (1:4 molar ratio). Large chemical shift changes at Leu-39, Val-49, and Leu-65 (Fig. 8*C*) indicated a potential binding site at the C-terminal tail, whereas the central TM region did not experience any change. Overall, these data suggest that E_{TR} has a structure in SDS/DPC micelles that is similar to the native fold of E_{FL} in biological membranes.

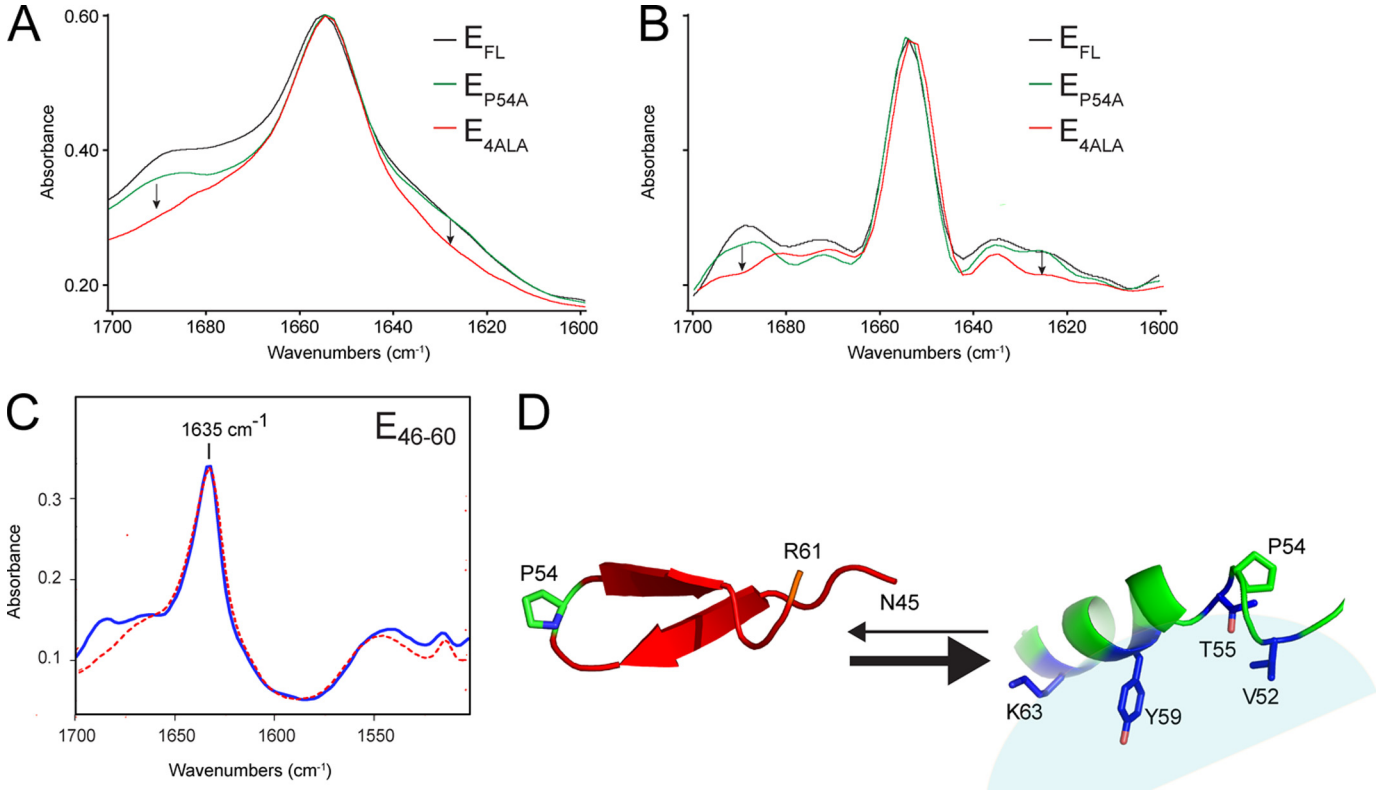

FIGURE 9. **Structural flexibility at the putative β-coil-β motif.** *A*, amide I band corresponding to E_{FL}, E_{P54A}, and E_{4ALA} in DMPC bilayers. Regions that change after mutation of the four residues indicated in Fig. 1*A* (E_{4ALA}) are shown as *arrows*. *B*, Fourier self-deconvolved spectra corresponding to the amide I bands shown in *A*. *C*, infrared amide I and II bands corresponding to SARS-CoV E peptide E_{46-60} in DMPC lipid bilayers before (*blue*) and after (*red*) being exposed to D_2O (39). *D*, possible equilibrium between two conformations at the putative β-coil-β motif, shifted toward an α-helical form, between the model determined experimentally for E_{TR} and E_{FL} and one built with prediction tools (PEP FOLD) (3) and consistent with data obtained with synthetic fragment E_{46-60} shown in *C*.

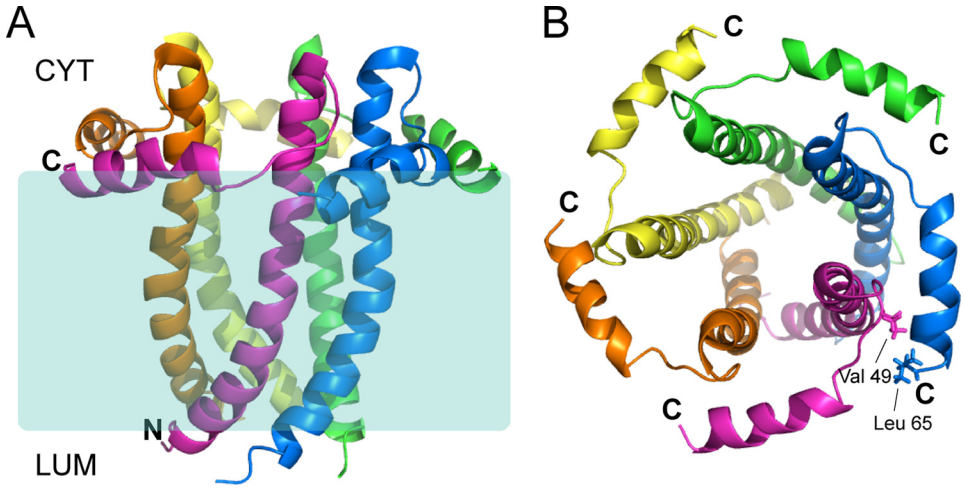

FIGURE 10. **Pentameric model formed by E_{TR}.** *Side* (*A*) and *top* (*B*) views of a proposed E_{TR} pentamer structure shown in *ribbon representations*. The side chains of Val-49 and Leu-65, which have been shown to interact with HMA, are shown as *line representations*.

Structural Discordance at the C-terminal Tail—Having determined the suitability of the construct used by comparison with the full-length protein and shown that the nature of the detergent did not affect the secondary structure significantly, we investigated the structure of the C-terminal extramembrane domain of E_{TR} and its apparent contrast with secondary structure predictions.

The secondary structure predictions clearly suggest the presence of a β-turn-β motif in the C-terminal region, not only in SARS-CoV E but also in other representative sequences of other coronaviruses (see Fig. 1*A*). Indeed, we have reported previously that the synthetic peptide E_{46-60}, which encompasses this putative β-hairpin, folds as β-strands, is completely resistant to H/D exchange, and has a very high tendency to aggregate in solution (39). However, we have shown here that in the context of E_{FL} or E_{TR}, this domain does not adopt a β-structure. To test if at least some part of the population adopts this structure in lipid membranes, we mutated E_{FL} residues 56–59 to increase the predicted helicity of this part of the molecule (43), from β-branched Val or bulky Tyr to small side chain Ala,

to obtain the construct E_{4ALA}. Last, to test the effect of the conserved Pro-54 at the center of this putative motif, we generated the mutant E_{P54A}.

The IR spectrum of these mutants when reconstituted in DMPC membranes (Fig. 9*A*) shows a similar amide I band. However, for the mutant E_{4ALA}, two shoulders are eliminated (see *arrows*). This indicates that these shoulders in E_{FL} do not represent misfolded protein, but they may correspond to the *bona fide* β-structure conformation present in a small part of the population. However, the significance of these mutations is not completely clear because, although the mutations introduced in E_{4ALA} prevented Golgi complex accumulation when the C terminus tail of SARS-E was coupled to VSV-G (43), a similar effect was also observed for the P54A mutant, which in our IR spectrum showed no obvious differences with respect to E_{FL}.

As stated above, the synthetic peptide E_{46-60} (39), which encompasses the predicted β-hairpin in SARS-CoV E, was found to produce ~100% β-structure and was completely resistant to H/D exchange (Fig. 9*C*). Combined with the effect observed for the E_{4ALA} mutant, we propose that this β structure may be in dynamic equilibrium with the much more abundant α-helical form (Fig. 9*D*). A delicate balance between these two forms may alter processes in the infected cell (*e.g.* membrane scission, binding to protein partners, or E protein localization).

Finally, the HMA titration results showed large CSP values for residues Val-49 and Leu-65, which are far apart in the sequence. Using the SymmDock server (75, 76), a reconstructed E_{TR} pentameric model was obtained based on the published structure of the E-TM pentamer (34) and the current E_{TR} structure. The model suggests that these two residues may be in fact spatially close (Fig. 10) and belong to different monomers, providing a rationale for the observation above.

CoV E proteins have been proposed to have at least two roles. One is related to their TM channel domain. This would be active in the secretory pathway, altering lumenal environments and rearranging secretory organelles and leading to efficient trafficking of virions (38, 77). The other would be related to their extramembrane domains, particularly the C-terminal domain. This is involved in protein-protein interactions and targeting, among other roles.

E protein participates in M-M and E-M interactions (17, 44), which are interesting targets for drug discovery. Also, formation of viral particles appears to be facilitated by a broad range of E sequences (78), which suggests that a common topology is more important than sequence requirements. E proteins have been suggested to act as chaperones during packaging (79), but the precise mechanism by which this takes place is not known. In this context, the structure determined here sheds light on a critical domain present in most CoV E proteins.

Acknowledgments—We thank T. Cornvik, A. Oi, and E. K. M. Nilsson (Nanyang Technological University/School of Biological Sciences Protein Production Platform) for the expression and screening of truncated SARS-CoV E constructs, Luis Enjuanes for the kind gift of the plasmid carrying nsp3a cDNA, and Yin Hoe Yau and Susana Geifman Shochat for guidance in conducting surface plasmon resonance experiments.

REFERENCES

1. González, J. M., Gomez-Puertas, P., Cavanagh, D., Gorbalenya, A. E., and Enjuanes, L. (2003) A comparative sequence analysis to revise the current taxonomy of the family Coronaviridae. *Arch. Virol.* **148,** 2207–2235
2. Enjuanes, L., Brian, D., Cavanagh, D., Holmes, K., Lai, M. M. C., Laude, H., Masters, P., Rottier, P., Siddell, S. G., Spaan, W. J. M., Taguchi, F., and Talbot, P. (2000) in *Virus Taxonomy: Classification and Nomenclature of Viruses* (van Regenmortel, M. H. V., Fauquet, C. M., Bishop, D. H. L., Carsten, E. B., Estes, M. K., Lemon, S. M., McGeoch, D. J., Maniloff, J., Mayo, M. A., Pringle, C. R., and Wickner, R. B., eds) pp. 835–849, Academic Press, Inc., San Diego
3. Maupetit, J., Derreumaux, P., and Tuffery, P. (2009) PEP-FOLD: an online resource for *de novo* peptide structure prediction. *Nucleic Acids Res.* **37,** W498–W503
4. Siddell, S. G. (1995) *The Coronaviridae: An Introduction*, Plenum Press, New York, NY
5. Gorbalenya, A. E., Snijder, E. J., and Spaan, W. J. (2004) Severe acute respiratory syndrome coronavirus phylogeny: toward consensus. *J. Virol.* **78,** 7863–7866
6. Kasai, T. (2007) Crisis management for infectious disease: learn from SARS experience and prepare for the influenza pandemic (Summary). *Japan Med. Assoc. J.* **50,** 117
7. Corman, V. M., Muller, M. A., Costabel, U., Timm, J., Binger, T., Meyer, B., Kreher, P., Lattwein, E., Eschbach-Bludau, M., Nitsche, A., Bleicker, T., Landt, O., Schweiger, B., Drexler, J. F., Osterhaus, A. D., Haagmans, B. L., Dittmer, U., Bonin, F., Wolff, T., and Drosten, C. (2012) Assays for laboratory confirmation of novel human coronavirus (hCoV-EMC) infections. *Eurosurveillance* **17,** 2–10
8. van Boheemen, S., de Graaf, M., Lauber, C., Bestebroer, T. M., Raj, V. S., Zaki, A. M., Osterhaus, A. D. M. E., Haagmans, B. L., Gorbalenya, A. E., Snijder, E. J., and Fouchier, R. A. (2012) Genomic characterization of a newly discovered coronavirus associated with acute Respiratory distress syndrome in humans. *MBio* 10.1128/mBio.00473-12
9. Muller, M. A., Raj, V. S., Muth, D., Meyer, B., Kallies, S., Smits, S. L., Wollny, R., Bestebroer, T. M., Specht, S., Suliman, T., Zimmermann, K., Binger, T., Eckerle, I., Tschapka, M., Zaki, A. M., Osterhaus, A. D. M. E., Fouchier, R. A. M., Haagmans, B. L., and Drosten, C. (2012) Human coronavirus EMC does not require the SARS-coronavirus receptor and maintains broad replicative capability in mammalian cell lines. *MBio* 10.1128/mBio.00515-12
10. Zaki, A. M., van Boheemen, S., Bestebroer, T. M., Osterhaus, A. D., and Fouchier, R. A. (2012) Isolation of a novel coronavirus from a man with pneumonia in Saudi Arabia. *N. Engl. J. Med.* **367,** 1814–1820
11. Anderson, L. J., and Baric, R. S. (2012) Emerging human coronaviruses: disease potential and preparedness. *N. Engl. J. Med.* **367,** 1850–1852
12. Al-Ahdal, M. N., Al-Qahtani, A. A., and Rubino, S. (2012) Coronavirus respiratory illness in Saudi Arabia. *J. Infect. Dev. Ctries.* **6,** 692–694
13. Nieto-Torres, J. L., Dediego, M. L., Alvarez, E., Jiménez-Guardeno, J. M., Regla-Nava, J. A., Llorente, M., Kremer, L., Shuo, S., and Enjuanes, L. (2011) Subcellular location and topology of severe acute respiratory syndrome coronavirus envelope protein. *Virology* **415,** 69–82
14. Bos, E. C., Luytjes, W., van der Meulen, H. V., Koerten, H. K., and Spaan, W. J. (1996) The production of recombinant infectious DI-particles of a murine coronavirus in the absence of helper virus. *Virology* **218,** 52–60
15. Corse, E., and Machamer, C. E. (2000) Infectious bronchitis virus E protein is targeted to the Golgi complex and directs release of virus-like particles. *J. Virol.* **74,** 4319–4326
16. Vennema, H., Godeke, G. J., Rossen, J. W., Voorhout, W. F., Horzinek, M. C., Opstelten, D. J., and Rottier, P. J. (1996) Nucleocapsid-independent assembly of coronavirus-like particles by co-expression of viral envelope protein genes. *EMBO J.* **15,** 2020–2028
17. Baudoux, P., Carrat, C., Besnardeau, L., Charley, B., and Laude, H. (1998) Coronavirus pseudoparticles formed with recombinant M and E proteins induce α interferon synthesis by leukocytes. *J. Virol.* **72,** 8636–8643
18. Corse, E., and Machamer, C. E. (2003) The cytoplasmic tails of infectious bronchitis virus E and M proteins mediate their interaction. *Virology* **312,** 25–34

19. Mortola, E., and Roy, P. (2004) Efficient assembly and release of SARS coronavirus-like particles by a heterologous expression system. *FEBS Lett.* **576,** 174–178
20. Fischer, F., Stegen, C. F., Masters, P. S., and Samsonoff, W. A. (1998) Analysis of constructed E gene mutants of mouse hepatitis virus confirms a pivotal role for E protein in coronavirus assembly. *J. Virol.* **72,** 7885–7894
21. Curtis, K. M., Yount, B., and Baric, R. S. (2002) Heterologous gene expression from transmissible gastroenteritis virus replicon particles. *J. Virol.* **76,** 1422–1434
22. Ortego, J., Escors, D., Laude, H., and Enjuanes, L. (2002) Generation of a replication-competent, propagation-deficient virus vector based on the transmissible gastroenteritis coronavirus genome. *J. Virol.* **76,** 11518–11529
23. DeDiego, M. L., Alvarez, E., Almazán, F., Rejas, M. T., Lamirande, E., Roberts, A., Shieh, W. J., Zaki, S. R., Subbarao, K., and Enjuanes, L. (2007) A severe acute respiratory syndrome coronavirus that lacks the E gene is attenuated *in vitro* and *in vivo*. *J. Virol.* **81,** 1701–1713
24. Dediego, M. L., Pewe, L., Alvarez, E., Rejas, M. T., Perlman, S., and Enjuanes, L. (2008) Pathogenicity of severe acute respiratory coronavirus deletion mutants in hACE-2 transgenic mice. *Virology* **376,** 379–389
25. DeDiego, M. L., Nieto-Torres, J. L., Jimenez-Guardeno, J. M., Regla-Nava, J. A., Alvarez, E., Oliveros, J. C., Zhao, J., Fett, C., Perlman, S., and Enjuanes, L. (2011) Severe acute respiratory syndrome coronavirus envelope protein regulates cell stress response and apoptosis. *PLoS Pathol.* 10.1371/journal.ppat.1002315
26. Enjuanes, L., Nieto-Torres, J. L., Jimenez-Guardeno, J. M., and DeDiego, M. L. (2011) in *Replicating Vaccines: Birkhauser Advances in Infectious Diseases* (Dormitzer, P. R., Mandl, C. W., and Rappuoli, R., eds) pp. 73–97, Springer, Basel, Switzerland
27. Netland, J., DeDiego, M. L., Zhao, J., Fett, C., Alvarez, E., Nieto-Torres, J. L., Enjuanes, L., and Perlman, S. (2010) Immunization with an attenuated severe acute respiratory syndrome coronavirus deleted in E protein protects against lethal respiratory disease. *Virology* **399,** 120–128
28. Lamirande, E. W., DeDiego, M. L., Roberts, A., Jackson, J. P., Alvarez, E., Sheahan, T., Shieh, W. J., Zaki, S. R., Baric, R., Enjuanes, L., and Subbarao, K. (2008) A live attenuated SARS coronavirus is immunogenic and efficacious in golden Syrian hamsters. *J. Virol.* **82,** 7721–7724
29. Torres, J., Maheswari, U., Parthasarathy, K., Ng, L., Liu, D. X., and Gong, X. (2007) Conductance and amantadine binding of a pore formed by a lysine-flanked transmembrane domain of SARS coronavirus envelope protein. *Protein Sci.* **16,** 2065–2071
30. Wilson, L., Gage, P., and Ewart, G. (2006) Hexamethylene amiloride blocks E protein ion channels and inhibits coronavirus replication. *Virology* **353,** 294–306
31. Wilson, L., McKinlay, C., Gage, P., and Ewart, G. (2004) SARS coronavirus E protein forms cation-selective ion channels. *Virology* **330,** 322–331
32. Torres, J., Parthasarathy, K., Lin, X., Saravanan, R., Kukol, A., and Liu, D. X. (2006) Model of a putative pore: the pentameric α-helical bundle of SARS coronavirus E protein in lipid bilayers. *Biophys. J.* **91,** 938–947
33. Torres, J., Wang, J., Parthasarathy, K., and Liu, D. X. (2005) The transmembrane oligomers of coronavirus protein E. *Biophys. J.* **88,** 1283–1290
34. Pervushin, K., Tan, E., Parthasarathy, K., Xin, L., Jiang, F. L., Yu, D., Vararattanavech, A., Soong, T. W., Liu, D. X., and Torres, J. (2009) Structure and inhibition of the SARS coronavirus envelope protein ion channel. *PLoS Pathol.* 10.1371/journal.ppat.1000511
35. Verdiá-Baguena, C., Nieto-Torres, J. L., Alcaraz, A., DeDiego, M. L., Torres, J., Aguilella, V. M., and Enjuanes, L. (2012) Coronavirus E protein forms ion channels with functionally and structurally-involved membrane lipids. *Virology* **432,** 485–494
36. Parthasarathy, K., Ng, L., Lin, X., Liu, D. X., Pervushin, K., Gong, X., and Torres, J. (2008) Structural flexibility of the pentameric SARS coronavirus envelope protein ion channel. *Biophys. J.* **95,** L39–L41
37. Corse, E., and Machamer, C. E. (2002) The cytoplasmic tail of infectious bronchitis virus E protein directs Golgi targeting. *J. Virol.* **76,** 1273–1284
38. Ruch, T. R., and Machamer, C. E. (2011) The hydrophobic domain of infectious bronchitis virus E protein alters the host secretory pathway and is important for release of infectious virus. *J. Virol.* **85,** 675–685
39. Surya, W., Samsó, M., and Torres, J. (2013) in *Respiratory Disease and Infection: A New Insight* (Vats, M., ed) pp. 47–76, InTech, Rijeka, Croatia
40. Hernandez, L. D., and White, J. M. (1998) Mutational analysis of the candidate internal fusion peptide of the avian leukosis and sarcoma virus subgroup a envelope glycoprotein. *J. Virol.* **72,** 3259–3267
41. Ito, H., Watanabe, S., Sanchez, A., Whitt, M. A., and Kawaoka, Y. (1999) Mutational analysis of the putative fusion domain of Ebola virus glycoprotein. *J. Virol.* **73,** 8907–8912
42. Wolfsberg, T. G., Straight, P. D., Gerena, R. L., Huovila, A. P., Primakoff, P., Myles, D. G., and White, J. M. (1995) ADAM, a widely distributed and developmentally regulated gene family encoding membrane proteins with a disintegrin and metalloprotease domain. *Dev. Biol.* **169,** 378–383
43. Cohen, J. R., Lin, L. D., and Machamer, C. E. (2011) Identification of a Golgi complex-targeting signal in the cytoplasmic tail of the severe acute respiratory syndrome coronavirus envelope protein. *J. Virol.* **85,** 5794–5803
44. Lim, K. P., and Liu, D. X. (2001) The missing link in coronavirus assembly. Retention of the avian coronavirus infectious bronchitis virus envelope protein in the pre-Golgi compartments and physical interaction between the envelope and membrane proteins. *J. Biol. Chem.* **276,** 17515–17523
45. Hogue, B. G., and Machamer, C. E. (2008) in *Nidoviruses* (Perlman, S., Gallagher, T., Snijder, E. J., eds) pp. 179–200, American Society for Microbiology Press, Washington, D. C.
46. de Haan, C. A., Vennema, H., and Rottier, P. J. (2000) Assembly of the coronavirus envelope: homotypic interactions between the M proteins. *J. Virol.* **74,** 4967–4978
47. Teoh, K. T., Siu, Y. L., Chan, W. L., Schlüter, M. A., Liu, C. J., Peiris, J. S., Bruzzone, R., Margolis, B., and Nal, B. (2010) The SARS coronavirus E protein interacts with PALS1 and alters tight junction formation and epithelial morphogenesis. *Mol. Biol. Cell* **21,** 3838–3852
48. Snijder, E. J., Bredenbeek, P. J., Dobbe, J. C., Thiel, V., Ziebuhr, J., Poon, L. L., Guan, Y., Rozanov, M., Spaan, W. J., and Gorbalenya, A. E. (2003) Unique and conserved features of genome and proteome of SARS-coronavirus, an early split-off from the coronavirus group 2 lineage. *J. Mol. Biol.* **331,** 991–1004
49. Alvarez, E., DeDiego, M. L., Nieto-Torres, J. L., Jiménez-Guardeno, J. M., Marcos-Villar, L., and Enjuanes, L. (2010) The envelope protein of severe acute respiratory syndrome coronavirus interacts with the non-structural protein 3 and is ubiquitinated. *Virology* **402,** 281–291
50. Marley, J., Lu, M., and Bracken, C. (2001) A method for efficient isotopic labeling of recombinant proteins. *J. Biomol. NMR* **20,** 71–75
51. Gan, S. W., Vararattanavech, A., Nordin, N., Eshaghi, S., and Torres, J. (2011) A cost-effective method for simultaneous homo-oligomeric size determination and monodispersity conditions for membrane proteins. *Anal. Biochem.* **416,** 100–106
52. Kauppinen, J. K., Moffatt, D. J., Cameron, D. G., and Mantsch, H. H. (1981) Noise in Fourier self-deconvolution. *Appl. Opt.* **20,** 1866–1879
53. Kochendoerfer, G. G., Salom, D., Lear, J. D., Wilk-Orescan, R., Kent, S. B., and DeGrado, W. F. (1999) Total chemical synthesis of the integral membrane protein influenza A virus M2: role of its C-terminal domain in tetramer assembly 1. *Biochemistry* **38,** 11905–11913
54. Schuck, P. (2003) On the analysis of protein self-association by sedimentation velocity analytical ultracentrifugation. *Anal. Biochem.* **320,** 104–124
55. Whitmore, L., and Wallace, B. A. (2004) DICHROWEB, an online server for protein secondary structure analyses from circular dichroism spectroscopic data. *Nucleic Acids Res.* **32,** W668–W673
56. Compton, L. A., and Johnson, W. C. (1986) Analysis of protein circular-dichroism spectra for secondary structure using a simple matrix multiplication. *Anal. Biochem.* **155,** 155–167
57. Abdul-Gader, A., Miles, A. J., and Wallace, B. A. (2011) A reference dataset for the analyses of membrane protein secondary structures and transmembrane residues using circular dichroism spectroscopy. *Bioinformatics* **27,** 1630–1636
58. Tycko, R., Blanco, F. J., and Ishii, Y. (2000) Alignment of biopolymers in strained gels: a new way to create detectable dipole-dipole couplings in high-resolution biomolecular NMR. *J. Am. Chem. Soc.* **122,** 9340–9341
59. Ulmer, T. S., Ramirez, B. E., Delaglio, F., and Bax, A. (2003) Evaluation of backbone proton positions and dynamics in a small protein by liquid crys-

tal NMR spectroscopy. *J. Am. Chem. Soc.* **125,** 9179–9191
60. Dosset, P., Hus, J. C., Marion, D., and Blackledge, M. (2001) A novel interactive tool for rigid-body modeling of multi-domain macromolecules using residual dipolar couplings. *J. Biomol. NMR* **20,** 223–231
61. Cornilescu, G., Delaglio, F., and Bax, A. (1999) Protein backbone angle restraints from searching a database for chemical shift and sequence homology. *J. Biomol. NMR* **13,** 289–302
62. Liang, B., Bushweller, J. H., and Tamm, L. K. (2006) Site-directed parallel spin-labeling and paramagnetic relaxation enhancement in structure determination of membrane proteins by solution NMR spectroscopy. *J. Am. Chem. Soc.* **128,** 4389–4397
63. Battiste, J. L., and Wagner, G. (2000) Utilization of site-directed spin labeling and high-resolution heteronuclear nuclear magnetic resonance for global fold determination of large proteins with limited nuclear overhauser effect data. *Biochemistry* **39,** 5355–5365
64. Van Horn, W. D., Beel, A. J., Kang, C., and Sanders, C. R. (2010) The impact of window functions on NMR-based paramagnetic relaxation enhancement measurements in membrane proteins. *Biochim. Biophys. Acta* **1798,** 140–149
65. Güntert, P., Mumenthaler, C., and Wüthrich, K. (1997) Torsion angle dynamics for NMR structure calculation with the new program DYANA. *J. Mol. Biol.* **273,** 283–298
66. Herrmann, T., Güntert, P., and Wüthrich, K. (2002) Protein NMR structure determination with automated NOE assignment using the new software CANDID and the torsion angle dynamics algorithm DYANA. *J. Mol. Biol.* **319,** 209–227
67. Brunger, A. T. (2007) Version 1.2 of the crystallography and NMR system. *Nat. Protoc.* **2,** 2728–2733
68. Brünger, A. T., Adams, P. D., Clore, G. M., DeLano, W. L., Gros, P., Grosse-Kunstleve, R. W., Jiang, J. S., Kuszewski, J., Nilges, M., Pannu, N. S., Read, R. J., Rice, L. M., Simonson, T., and Warren, G. L. (1998) Crystallography & NMR system: a new software suite for macromolecular structure determination. *Acta Crystallogr. D Biol. Crystallogr.* **54,** 905–921
69. Serrano, P., Johnson, M. A., Almeida, M. S., Horst, R., Herrmann, T., Joseph, J. S., Neuman, B. W., Subramanian, V., Saikatendu, K. S., Buchmeier, M. J., Stevens, R. C., Kuhn, P., and Wüthrich, K. (2007) Nuclear magnetic resonance structure of the N-terminal domain of nonstructural protein 3 from the severe acute respiratory syndrome coronavirus. *J. Virol.* **81,** 12049–12060
70. Myszka, D. G. (1999) Improving biosensor analysis. *J. Mol. Recognit.* **12,** 279–284
71. Parthasarathy, K., Lu, H., Surya, W., Vararattanavech, A., Pervushin, K., and Torres, J. (2012) Expression and purification of coronavirus envelope proteins using a modified β-barrel construct. *Protein Expression Purification* **85,** 133–141
72. Spera, S., and Bax, A. (1991) Empirical correlation between protein backbone conformation and Cα and Cβ ^{13}C nuclear magnetic resonance chemical shifts. *J. Am. Chem. Soc.* **113,** 5490–5492
73. Xu, X.-P., and Case, D. A. (2001) Automated prediction of ^{15}N, ^{13}Cα, ^{13}Cβ and ^{13}C′ chemical shifts in proteins using a density functional database. *J. Biomol. NMR* **21,** 321–333
74. Fleming, K. G. (2002) Standardizing the free energy change of transmembrane helix-helix interactions. *J. Mol. Biol.* **323,** 563–571
75. Schneidman-Duhovny, D., Inbar, Y., Nussinov, R., and Wolfson, H. J. (2005) Geometry-based flexible and symmetric protein docking. *Proteins* **60,** 224–231
76. Schneidman-Duhovny, D., Inbar, Y., Nussinov, R., and Wolfson, H. J. (2005) PatchDock and SymmDock: servers for rigid and symmetric docking. *Nucleic Acids Res.* **33,** W363–W367
77. Ruch, T. R., and Machamer, C. E. (2012) A single polar residue and distinct membrane topologies impact the function of the infectious bronchitis coronavirus E protein. *PLoS Pathol.* 10.1371/journal.ppat.1002674
78. Kuo, L., Hurst, K. R., and Masters, P. S. (2007) Exceptional flexibility in the sequence requirements for coronavirus small envelope protein function. *J. Virol.* **81,** 2249–2262
79. Kuo, L., and Masters, P. S. (2010) Evolved variants of the membrane protein can partially replace the envelope protein in murine coronavirus assembly. *J. Virol.* **84,** 12872–12885